

Granger Causal Chain Discovery for Sepsis-Associated Derangements via Multivariate Hawkes Processes

Song Wei^a Yao Xie^a Christopher S. Josef^b Rishikesan Kamaleswaran^{c,d}

^aSchool of Industrial and Systems Engineering, Georgia Institute of Technology.

^bDepartment of Surgery, Emory University School of Medicine.

^cDepartment of Biomedical Informatics, Emory University School of Medicine.

^dDepartment of Biomedical Engineering, Georgia Institute of Technology.

Abstract

Modern health care systems are conducting continuous, automated surveillance of the electronic medical record (EMR) to identify adverse events with increasing frequency; however, many events such as sepsis do not have clearly elucidated prodromes (i.e., event chains) that can be used to identify and intercept the adverse event early in its course. Currently there does not exist a reliable framework for discovering or describing causal chains that precede adverse hospital events. Clinically relevant and interpretable results require a framework that can (1) infer temporal interactions across multiple patient features found in EMR data (e.g., labs, vital signs, etc.) and (2) can identify pattern(s) which precede and are specific to an impending adverse event (e.g., sepsis). In this work, we propose a linear multivariate Hawkes process model, coupled with $g(x) = x^+$ link function to allow potential inhibition effects, in order to recover a Granger Causal (GC) graph. We develop a two-phase gradient-based scheme to maximize a surrogate of likelihood to estimate the problem parameters. This two-phase algorithm is scalable and shown to be effective via our numerical simulation. It is subsequently extended to a data set of patients admitted to Grady hospital system in Atlanta, GA, where the fitted Granger Causal graph identifies several highly interpretable chains that precede sepsis.

Keywords: EMR; Granger Causality; Multivariate Hawkes process; Sepsis-Associated Derangement (SAD).

1 Introduction

Continuous, automated surveillance systems that use machine learning models to identify adverse patient events are being incorporated into healthcare environments with increasing frequency. One of the most notable adverse events is sepsis, a life-threatening medical condition contributing to one in five deaths globally [WHO, 2020] and stands as one of the most important cases for automated in-hospital surveillance. Sepsis is formally defined as life-threatening organ dysfunction caused by a dysregulated host response to infection [Singer et al., 2016]. Delays in recognizing sepsis and initiating appropriate treatment can adversely impact patient outcomes. In a recent study of adult sepsis patients, each hour of delayed treatment was associated with higher risk-adjusted in-hospital mortality (odds ratio, 1.04 per hour) [Seymour et al., 2017]. It logically follows that early recognition of the physiologic aberrations preceding sepsis would afford clinicians more time to intervene and may contribute to improving outcomes and reducing costs. Many machine learning methods have been developed to predict the onset of sepsis, utilizing data from the electronic medical record (EMR) [Fleuren et al., 2020, Reyna et al., 2019, Shashikumar et al., 2021]. While many approaches can be designed to provide an alert preceding an event, most are not designed to discover and report the causal chains that preceded an adverse event. Developing and reporting a causal chain of events not only serves as a foundation for prognosticating adverse event occurrence, but more importantly it reveals the pathways of deterioration which may afford clinicians the additional context to corroborate or modify existing treatment modalities in a way that is superior to a simple alarm.

Recently, Hawkes processes [Hawkes, 1971a,b, Hawkes and Oakes, 1974], which model self- and mutual- exciting patterns among continuous-time events, have drawn a lot of attention in the field of health analytics [Meyer and Held, 2014, Choi et al., 2015, Bao et al., 2017, Schoenberg et al., 2019, Wei et al., 2021a]. In our problem, a linear multivariate Hawkes process (MHP) seems appealing, since (1) the support of the excitation matrix enjoys a natural interpretation as a Granger Causal (GC) graph [Xu et al., 2016], (2) given its interpretation as a clustering process [Hawkes and Oakes, 1974], we can infer the commonly observed chain pattern that precedes sepsis from the learned GC graph, and (3) with proper domain expertise, simple methods, such as (generalized) linear model, are proven effective in outputting highly explainable results [Choi et al., 2015, Wei et al., 2021a].

However, there are two major challenges preventing us from applying linear MHP to recover the GC graph. First and foremost, without a non-linear link function, linear MHP itself fails to model inhibiting effects (e.g., proper medication will inhibit occurrence of a certain disease), since “negative triggering effect” could lead to negative conditional intensity and thus intractable likelihood.

Second, a well-established expectation–maximization (EM) based stochastic declustering algorithm [Zhuang et al., 2002, Fox et al., 2016] suffers from scalability issue and cannot be applied to EMR data with thousands of patients’ trajectories. One common solution to the first challenge is adopting a non-linear link function, e.g., exponential link, which maps all negative values to non-negative ones. Recently, Bonnet et al. [2022] adopt $g(x) = x^+ := \max\{0, x\}$ link function. To evaluate and maximize likelihood, they calculate the “re-start” time, at which the conditional intensity becomes nonzero. However, such a calculation has quadratic complexity, making it unscalable. Scalable methods to infer GC graph with both exciting and inhibiting effects for MHP are still largely missing.

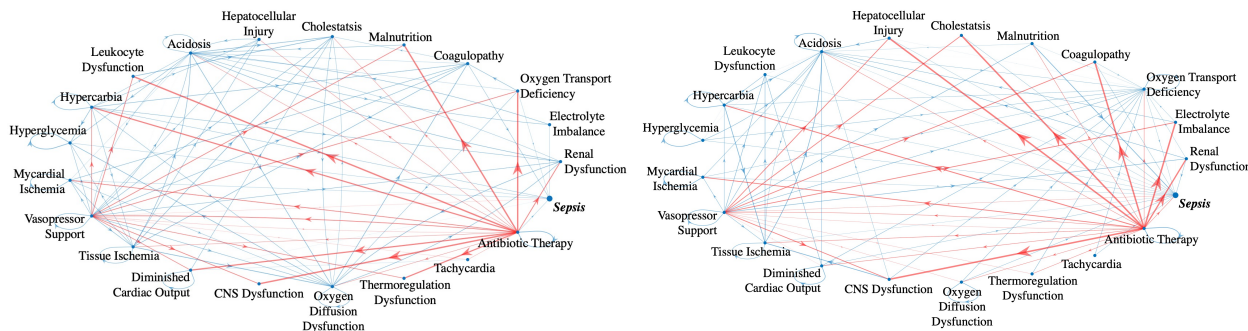


Figure 1: Granger Causal graphs over Sepsis-Associated Derangement fitted on Sepsis-3 patient cohort (left) and full patient cohort (right) via linear multivariate Hawkes processes.

Contribution. In this paper, we adopt $g(x) = x^+$ link function in MHP, in order to recover a GC graph with both exciting and inhibiting effects. The contribution is three-fold. Firstly, we propose to maximize a surrogate of the true likelihood, which is essentially the likelihood of the linear MHP (i.e., we remove the non-differentiable link in the conditional intensity). The reason is three-fold: (i) within the feasible region, this surrogate serves as a good approximation to the true likelihood; (ii) the gradient field of this surrogate enjoys a simple closed-form evaluation, which makes the powerful yet simple gradient-based method applicable; (iii) even though this gradient field is not the gradient of true likelihood, it enjoys an interpretation as a strong monotone vector field [Juditsky and Nemirovski, 2019, Juditsky et al., 2020, Wei et al., 2021b], which may explain its empirical success.

Secondly, we develop a scalable two-phase gradient-based algorithm¹ coupled with a proper learning rate decaying scheme based on the gradient norm to solve the optimization problem. Our proposed algorithm fixes (i) the unscalability issue of projected gradient descent (GD), which is similar to the “re-start” time method [Bonnet et al., 2021, 2022]; (ii) the divergence issue of

¹Implementation is available at <https://github.com/SongWei-GT/two-phase-MHP>

vanilla GD due to potential inhibiting effect. Moreover, we use extensive numerical simulation to demonstrate our method’s empirical success.

Lastly, we report graphs (i.e., Figure 1) that afford clinicians a simple mechanism for interpreting both inhibitory and promoting causal relationship amongst the data. Networks are exceptionally important for syndromic (i.e. a constellation of different physiologic derangements can be manifested) conditions like sepsis. These graphs can be used to differentiate cohorts and to identify important, intra-cohort relationships. For clinicians the utility of these graphs is two fold: they can be used to (i) quantify a patient’s risk of developing subsequent physiologic derangements in the future and (ii) discover new relationships. The learned Granger causal graphs in this work are highly interpretable and can be used to create or augment surveillance systems for high-risk patients. Here, we demonstrate the effectiveness of our approach in learning a Granger causal graph over Sepsis Associated Derangements (SADs), but it can be generalized to other applications with similar requirements.

1.1 Related work

The study of Granger Causality in time series literature via vector autoregressive (VAR) time series has been a heated topic for years. Recent advancements mainly focus on non-linear dynamics [Sindhwani et al., 2012, Tank et al., 2018] and tackling high-dimensionality via regularization [Bolstad et al., 2011, Basu et al., 2015, 2019]. For a comprehensive survey of the recent development of Granger Causality in the context of time series, we refer readers to Shojaie and Fox [2021].

VAR models and mutivariate Hawkes process (MHP) models share many similarities and some have recently recognized that the self- and mutual- excitation matrix in the Hawkes process model can be interpreted as Granger Causal graph in a similar way. The study of GC under the context of MHP can be traced back to Kim et al. [2011]. Recent development includes leveraging alternating direction method of multipliers to infer the low-rank structure in mutual excitation matrix [Zhou et al., 2013], applying EM algorithm with various constraints [Xu et al., 2016, Chen et al., 2022, Ide et al., 2021] and using powerful neural networks [Zhang et al., 2020] to infer the GC graph.

Even outside the context of Granger Causality, estimation of MHP has been a research hotspot for years. The most famous method would be the stochastic declustering algorithm, which is based on the EM algorithm. Such algorithms have been applied to Hawkes process parameter estimation with various kernel functions, e.g., probability weighted kernel estimation with adaptive bandwidth [Zhuang et al., 2002], probability weighted histogram estimation [Marsan and Lengline, 2008] and with inhomogeneous spatial background rate [Fox et al., 2016], etc. In addition, there are also a lot of neural network based methods, including neural Hawkes process [Mei and Eisner, 2017],

Transformer Hawkes process [Zuo et al., 2020] and so on. Moreover, there are also recent attempts to explore powerful yet simple gradient-based method to infer the problem parameters; notable contributions include Wang et al. [2020], Cartea et al. [2021]. Here, we want to mention that the $g(x) = x^+$ link function is novel in literature [Bonnet et al., 2021, 2022]. Since there have not been many methods tailored to this particular parameterization, we only numerically compare our method with the re-start time method [Bonnet et al., 2021, 2022] and some naive gradient-based methods.

2 Background

2.1 Multivariate Hawkes Process

A counting process

$$N = (N^1, \dots, N^d),$$

where each process $N^i = \{N_t^i : t \in [0, T]\}$ itself is a counting measure on time horizon T and records the number of type- i events before time t , is called a multivariate linear Hawkes process (MHP) if the conditional intensity of i -th process ($i = 1, \dots, d$) is defined as follows

$$\lambda_i(t) = \mu_i + \sum_{j=1}^d \int_0^t \varphi_{i,j}(s) dN_{t-s}^j,$$

where μ_i is the exogenous background intensity for type- i event, independent of the history and kernel function $\varphi_{i,j}(\cdot)$ captures the impact from historical type- j event to subsequent type- i event.

In this work, we adopt a very common and popular kernel function — exponential kernel, i.e.,

$$\varphi_{i,j}(t) = \alpha_{i,j} \exp\{-\beta t\}.$$

Here, parameter $\alpha_{i,j}$ represents the magnitude of the impact from type- j event to type- i event and β characterizes the rate of decay of that impact. Most importantly, unlike classic model, we consider not only exciting effect, but also inhibiting effect by allowing negative magnitude parameters $\alpha_{i,j}$'s. However, this could lead to negative intensity, which contradicts the understanding of conditional intensity as the instantaneous probability of event occurrence. To fix this issue, we apply operator $(\cdot)^+ = \max\{0, \cdot\}$ to the linear conditional intensity [Bonnet et al., 2021] and get

$$\lambda_i(t) = \left(\mu_i + \sum_{j=1}^d \int_0^t \alpha_{i,j} e^{-\beta s} dN_{t-s}^j \right)^+. \quad (1)$$

We denote the background intensity vector as $\mu = (\mu_1, \dots, \mu_d)^T$ and excitation/inhibition matrix as $A = (\alpha_{i,j}) \in \mathbb{R}^{d \times d}$. We will show the support of matrix A enjoys a natural interpretation as a Granger Causal graph.

2.2 Granger causality

The notion of Granger Causality was introduced to multivariate Hawkes process by Eichler et al. [2017], Xu et al. [2016]. In the seminal paper, Eichler et al. [2017] showed that the Granger causal structure of the MHP is fully encoded in the excitation/inhibition matrix. Under our multivariate linear Hawkes process (with exponential decay kernel) model, the Granger Causality can be formally defined as follows:

Proposition 1 (Eichler et al. [2017]). Let $N = (N^1, \dots, N^d)$ be a d -dimensional multivariate Hawkes process with conditional intensity defined in (1), then N^j does NOT Granger-cause N^i if and only if $\alpha_{i,j} = 0$.

We need to remark that inferring Granger Causality needs “all the information in the universe” and hence we can only learn Granger non-causality and *prima facie causality* given partially observed data [Granger, 1969, 1980, 1988]. In the graph induced by the excitation/inhibition matrix $A = (\alpha_{i,j})$, the absence of an edge means Granger non-causality whereas the presence of an edge in A only implies *prima facie causality*. However, since unobserved confounding is outside the scope of this work, we will call this matrix A Granger causal graph, assuming that the observed information is “enough” to infer Granger Causality.

Moreover, this excitation/inhibition matrix A can be understood as a directed information graph (DIG) [Etesami et al., 2016], which is a generalized causal notion of Granger Causality. To be precise, in DIG, we determine the causality by comparing two conditional probabilities in KL-divergence sense: one is the conditional probability of N_{t+dt}^i given full history, and the other one is the conditional probability of N_{t+dt}^i given full history except that of type- j event. Last but not least, both Granger causal graph and DIG are equivalent to minimal generative model graphs [Quinn et al., 2011] and therefore can be used for causal inference in the same manner Bayesian networks are used for correlative statistical inference.

3 Estimation

Consider we observe a sequence of events over time horizon T :

$$(u_1, t_1), \dots, (u_N, t_N),$$

where $u_i \in \{1, \dots, d\}$ represents the type of the event and

$$0 \leq t_1 < \dots < t_N \leq T$$

denote the exact occurrence times of those events. The conditional intensity function of type- i event at time t is as follows:

$$\lambda_i(t) = \left(\mu_i + \sum_{j:t_j < t} \alpha_{i,u_j} e^{-\beta(t-t_j)} \right)^+.$$

Typically, we apply Maximum likelihood estimation (MLE) to learn model parameters, where the log-likelihood is defined as:

$$\ell(\mu, A; \beta) = \sum_{i=1}^d \left(\int_0^T \log \lambda_i(t) dN_t^i - \int_0^T \lambda_i(t) dt \right). \quad (2)$$

However, the $(\cdot)^+$ operator makes the above likelihood function non-differentiable. To leverage the powerful gradient method, we simply remove the $(\cdot)^+$ operator in the conditional intensity — we denote $\tilde{\lambda}_i(t) = \mu_i + \sum_{j:t_j < t} \alpha_{i,u_j} e^{-\beta(t-t_j)}$ and define a surrogate log-likelihood, which is an approximation to the true likelihood, as follows:

$$\tilde{\ell}(\mu, A; \beta) = \sum_{i=1}^d \left(\int_0^T \log \tilde{\lambda}_i(t) dN_t^i - \int_0^T \tilde{\lambda}_i(t) dt \right). \quad (3)$$

We say it is an approximation, since even for parameter (μ, A) within the feasible region

$$\Theta = \{(\mu, A) : \tilde{\lambda}_{u_n}(t_n) > 0, n = 1, \dots, N\}, \quad (4)$$

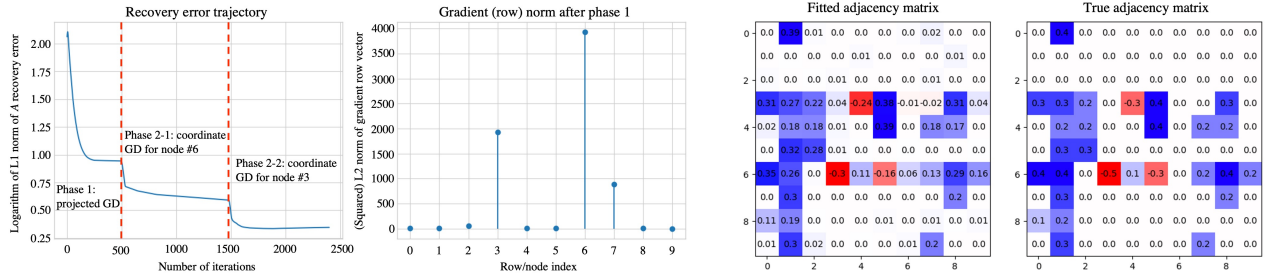
the values between true likelihood (2) and its surrogate (3) could differ since $\tilde{\lambda}_i(t)$ can be negative on some intervals. Nevertheless, this surrogate $\tilde{\ell}(\mu, A; \beta)$ enjoys a very simple closed-form expression:

$$\sum_{i=1}^d \sum_{j=1}^{N-1} \frac{\alpha_{i,u_j}}{\beta} (e^{-\beta(t_N-t_j)} - 1) - T \sum_{i=1}^d \mu_i + \sum_{n=1}^N \log \left(\mu_{u_n} + \sum_{j < n} \alpha_{u_n, u_j} e^{-\beta(t_n-t_j)} \right). \quad (5)$$

We will maximize this surrogate likelihood to estimate the problem parameters, i.e.,

$$\widehat{\mu}, \widehat{A} = \operatorname{argmin}_{\mu, A \in \Theta} -\widetilde{\ell}(\mu, A; \beta). \quad (6)$$

Since the objective function (6) is convex with respect to (w.r.t.) (μ, A) [Bacry et al., 2015], projected Gradient Descent (GD) is a tempting choice, which enjoys strong convergence guarantee. Despite the simple closed-form expression of $\widetilde{\lambda}_i(t)$, its evaluation as well as the projection back to Θ are computationally intense, making projected GD unscalable. Fortunately, the gradient field of this surrogate remains well-defined even outside the feasible region Θ , making the vanilla GD possible. However, vanilla GD (without projection) will suffer from divergence issue, as the iterate can easily go outside the feasible region Θ . Thus, we need to gradually decay the learning rate during the learning process. Since the (surrogate) log-likelihood is also intractable, it cannot be used to fulfill this purpose. To handle those difficulties, we propose a two-phase GD-based algorithm coupled with a learning rate decaying scheme based on the gradient norm; this algorithm is illustrated in Figure 2(a) and one can see its good performance in Figure 2(b). Next, we will briefly introduce this algorithm.



(a) Illustration of the two-phase algorithm. After Phase 1, we select nodes # 3 and # 6 (percentage threshold $p = 0.85$ in Algorithm 2), on which we further perform phase 2 batch coordinate GD.

(b) Demonstration of effectiveness of our proposed algorithm. The ℓ_1 norm of A recovery error is 1.4, and the Hamming distance and Structural Hamming distance between the true and fitted adjacency matrix A are both zeros.

Figure 2: Illustration of our proposed algorithm via a $d = 10$ toy example.

Phase 1: Projected Gradient Descent. In the first phase, we constrain all parameters to be non-negative and perform projected GD with fixed step length. We denote $\widehat{\mu}_t, \widehat{A}_t$ as iterates at t -th step

and the update rule is

$$\begin{aligned}\widehat{\mu}_t &\leftarrow \widehat{\mu}_{t-1} + \gamma \nabla_{\mu} \widetilde{\ell} / \|\nabla_{\mu} \widetilde{\ell}\|_2, \\ \widehat{A}_t &\leftarrow \widehat{A}_{t-1} + \gamma \nabla_A \widetilde{\ell} / \|\nabla_A \widetilde{\ell}\|_F,\end{aligned}$$

where γ is step size (learning rate), $\|\cdot\|_2$, $\|\cdot\|_F$ represent vector ℓ_2 norm and matrix Frobenius norm and the gradient fields are defined as: $\nabla_{\mu} \widetilde{\ell} = \nabla_{\mu} \widetilde{\ell}(\widehat{\mu}_{t-1}, \widehat{A}_{t-1}; \beta)$, $\nabla_A \widetilde{\ell} = \nabla_A \widetilde{\ell}(\widehat{\mu}_{t-1}, \widehat{A}_{t-1}; \beta)$. Here, parameter β is assumed to be known and in practice we will perform grid search to select the best β . In order to make sure we do not get negative intensity, we perform the following projection:

$$\begin{aligned}\widehat{\mu}_t &\leftarrow \operatorname{argmin}_{\mu \in \mathbb{R}_+} \|\widehat{\mu}_t - \mu\|_2, \\ \widehat{A}_t &\leftarrow \operatorname{argmin}_{A \in \mathbb{R}_+^{d \times d}} \|\widehat{A}_t - A\|_F,\end{aligned}$$

which can be easily achieved by setting all negative entries to zeros. Complete details of the project GD algorithm can be found in Algorithm 1 in Appendix A.

The advantage of this phase is three-fold: (1) it guides us to a neighborhood around the global optimizer and meanwhile (2) ensures the stability/convergence of the algorithm and (3) reduces the computation cost by finding a small batch of coordinates to further optimize (see Figure 2(a) and the description of phase 2 below).

Phase 2: Batch Coordinate Gradient Descent. In the second phase, we consider those nodes whose corresponding rows could have negative values. We identify those nodes by the ℓ_2 norm of the gradient (w.r.t. A) row vector — large value indicates that convergence of the corresponding row is not achieved after phase 1 (see the right panel in Figure 2(a)) and thus we should apply gradient descent without the constraint/projection to recover the parameters. See complete details on how to identify those rows in Algorithm 2. Last but not least, we only need to perform gradient descent for those selected rows in A (and corresponding background intensities). Despite intractable log-likelihood in this phase, we develop a learning rate decaying scheme based on the gradient F -norm in order to achieve convergence. Details of the algorithm can be found in Algorithm 3 in Appendix A.

Recently, Juditsky and Nemirovski [2019], Juditsky et al. [2020] showed that a projected GD along some (strong) monotone vector field can be interpreted as a solution to a stochastic variation inequality (VI) and enjoys both signal recovery guarantee and convergence guarantee. However, since we do not constraint the iterate within Θ in phase 2, the vector fields $\nabla_{\mu} \widetilde{\ell}$, $\nabla_A \widetilde{\ell}$ are no longer monotone. Hence, we could only use numerical evidence to demonstrate the effectiveness of

our method. Nevertheless, this vector field view under VI framework might give us a chance to theoretically explain our heuristic’s empirical success.

4 Numerical simulation

In this section, we will demonstrate the good performance of our proposed two-phase method (coupled with grid search for unknown β) via numerical simulation. We will use the likelihood at the end of phase 1 as the goodness-of-fit (GoF) criterion to select (hyper-)parameter β .

Table 1: Performance of proposed algorithm when β is unknown. The last row corresponds to selected β based on end-of-phase 1 log-likelihood, where we can observe its performance is almost the same with the optimal β ’s performance.

β	$d = 5$				$d = 10$				$d = 20$			
	μ err.*	A err.	A HD	A SHD	μ err.*	A err.	A HD	A SHD	μ err.*	A err.	A HD	A SHD
0.4	5.01 (3.16)	1.51 (0.85)	0.06 (0.092)	1.5 (2.3)	8.53 (3.81)	4.39 (0.63)	0.03 (0.052)	3.0 (5.27)	14.97 (5.13)	13.46 (2.14)	0.047 (0.044)	19.0 (17.82)
0.5	5.78 (3.3)	1.26 (0.86)	0.04 (0.08)	1.0 (2.01)	10.57 (4.39)	3.49 (0.6)	0.02 (0.033)	2.0 (3.39)	20.51 (6.16)	10.59 (2.27)	0.043 (0.047)	17.5 (18.88)
0.6	5.39 (3.24)	1.05 (0.88)	0.02 (0.071)	0.5 (1.79)	10.04 (4.36)	2.58 (0.64)	0.02 (0.023)	2.0 (2.38)	21.18 (6.41)	8.55 (2.35)	0.045 (0.046)	18.0 (18.67)
0.7	5.2 (3.12)	0.86 (0.88)	0.0 (0.065)	0.0 (1.64)	8.94 (4.05)	1.86 (0.61)	0.01 (0.024)	1.0 (2.47)	19.35 (6.09)	6.54 (2.43)	0.048 (0.048)	19.5 (19.24)
0.8	4.67 (3.02)	0.74 (0.89)	0.0 (0.039)	0.0 (0.99)	7.54 (3.74)	1.4 (0.46)	0.01 (0.018)	1.0 (1.85)	17.11 (5.65)	4.98 (2.5)	0.06 (0.053)	24.0 (21.52)
0.9	4.51 (2.94)	0.66 (0.9)	0.0 (0.036)	0.0 (0.91)	6.79 (3.53)	1.52 (0.41)	0.01 (0.02)	1.0 (2.08)	16.34 (5.21)	5.11 (2.13)	0.07 (0.055)	28.0 (22.32)
1	4.46 (2.87)	0.79 (0.92)	0.0 (0.034)	0.0 (0.86)	7.16 (3.47)	1.84 (0.39)	0.01 (0.022)	1.0 (2.28)	18.0 (5.29)	5.93 (1.82)	0.088 (0.055)	35.5 (22.29)
1.1	4.56 (2.79)	1.03 (0.91)	0.0 (0.035)	0.0 (0.87)	7.73 (3.47)	2.3 (0.34)	0.02 (0.026)	2.0 (2.65)	19.95 (5.55)	6.83 (1.64)	0.103 (0.056)	41.5 (22.52)
1.2	4.75 (2.74)	1.2 (1.22)	0.0 (0.032)	0.0 (0.85)	8.4 (3.46)	2.72 (0.38)	0.03 (0.033)	3.0 (3.36)	22.84 (6.08)	7.8 (1.53)	0.121 (0.052)	48.5 (21.1)
–	4.57 (2.96)	0.74 (0.89)	0.0 (0.036)	0.0 (0.9)	7.04 (3.55)	1.62 (0.41)	0.01 (0.021)	1.0 (2.17)	16.7 (5.34)	5.06 (2.19)	0.07 (0.055)	28.0 (22.02)

* the value times 10^{-2} is the true μ recovery error; we omit $\times 10^{-2}$ in the value due to space consideration.

Experiment 1. We perform grid search on $\beta \in \{0.4, 0.5, 0.6, 0.7, 0.8, 0.9, 1, 1.1, 1.2\}$ (ground truth is 0.8). For each grid value, we fit the model to randomly generated synthetic data (50 sequences with $T = 500$) and repeat this procedure independently for 100 times. At each trial, we select β with the largest end-of-phase 1 likelihood. We report (1) ℓ_1 norm of β recovery error (β err.), (2) ℓ_1 norm of μ recovery error (μ err.), (3) ℓ_1 norm of A recovery error (A err.), (4) Hamming Distance (A HD) and (5) Structural Hamming Distance (A SHD) between ground truth and fitted adjacency matrix A over 100 trials in Table 1. We can observe that the grid search approach achieves comparably good performance with the optimal and true parameter cases, which are all satisfying.

In addition, we also show that those errors will decrease with increasing sequence length T (or sequence number). To be precise, we study the behavior of those errors with respect to (w.r.t.) the time horizon T and total number of sequences, assuming that we know the ground truth β . We generate (1) one single sequence on time horizon $T \in \{500, 2000, 5000, 10000, 20000\}$ and (2) multiple sequences (total sequence number chosen from $\{1, 10, 20, 50, 100\}$) on time horizon $T = 500$ and learn the parameter via our proposed two-phase method. We report similar evaluation

metrics over 100 independent trials. The results for $d = 5, 10$ cases can be found in Table 2. We can see that with longer sequence (or more sequences), all those errors decrease monotonically, which further demonstrates the effectiveness of our proposed method.

Table 2: Consistency of our proposed two-phase algorithm when β is assumed to be known.

Varying Sequence Time Horizon T (Seq. Num. fixed to be 1).										
T	$d = 5$					$d = 10$				
	500	2000	5000	10000	20000	500	2000	5000	10000	20000
μ err.*	7.41 (3.42)	5.34 (2.93)	4.25 (2.76)	3.81 (2.8)	3.69 (2.72)	17.96 (5.98)	11.26 (4.47)	8.65 (4.01)	8.78 (3.8)	7.58 (3.75)
A err.	8.94 (5.96)	2.26 (2.81)	1.01 (0.82)	0.75 (0.43)	0.57 (0.23)	20.95 (12.55)	4.93 (2.55)	2.6 (1.04)	1.87 (0.61)	1.52 (0.48)
A HD	0.24 (0.13)	0.08 (0.091)	0.04 (0.076)	0.04 (0.059)	0.0 (0.056)	0.245 (0.075)	0.07 (0.063)	0.03 (0.035)	0.015 (0.025)	0.01 (0.018)
A SHD	6.0 (3.43)	2.0 (2.28)	1.0 (1.9)	1.0 (1.48)	0.0 (1.41)	24.5 (7.72)	7.0 (6.34)	3.0 (3.57)	1.5 (2.55)	1.0 (1.86)

Varying Sequence Number (Time Horizon T fixed to be 500).										
Seq. Num.	$d = 5$					$d = 10$				
	1	10	20	50	100	1	10	20	50	100
μ err.*	6.25 (3.29)	3.91 (2.81)	3.86 (2.72)	3.41 (2.66)	2.91 (2.50)	17.96 (5.98)	8.61 (4.01)	8.67 (3.78)	7.54 (3.74)	6.9 (3.49)
A err.	9.42 (5.50)	1.19 (1.22)	0.86 (1.00)	0.6 (0.91)	0.54 (0.91)	20.96 (12.56)	2.62 (1.04)	1.84 (0.61)	1.4 (0.46)	1.51 (0.47)
A HD	0.26 (0.120)	0.06 (0.075)	0.04 (0.061)	0.04 (0.045)	0.0 (0.050)	0.245 (0.075)	0.03 (0.036)	0.015 (0.026)	0.01 (0.018)	0.01 (0.017)
A SHD	7.0 (3.14)	1.5 (1.89)	1.0 (1.53)	1.0 (1.14)	0.0 (1.27)	24.5 (7.72)	3.0 (3.66)	1.5 (2.71)	1.0 (1.85)	1.0 (1.76)

* we omit $\times 10^{-2}$ in the value due to space consideration.

We also perform experiment for $d = 20$ case. We report the same evaluation metrics in Tables 3 and 4. However, due to the computational limitation, we only report the results for smaller number of sequences and shorter time horizons. Nevertheless, we can still see the decaying error pattern as observed in the above $d = 5, 10$ cases.

Table 3: Consistency w.r.t. Sequence Time Horizon T (Seq. Num. fixed to be 1)

T	500	2000	5000	10000
μ err.*	58.45 (19.23)	33.75 (11.3)	24.88 (8.87)	21.01 (7.67)
A err.	39.43 (15.93)	12.07 (4.14)	6.98 (2.26)	5.51 (2.19)
A HD	0.24 (0.064)	0.068 (0.051)	0.032 (0.037)	0.025 (0.044)
A SHD	96.0 (25.91)	27.5 (20.66)	13.0 (14.97)	10.0 (17.64)

* WE OMIT $\times 10^{-2}$ IN THE VALUE DUE TO SPACE CONSIDERATION.

Table 4: Consistency w.r.t. Sequence Number (Time Horizon $T = 500$)

SEQ. NUM.	1	10	20
μ err.*	57.91 (19.71)	24.16 (8.84)	20.34 (7.56)
A err.	39.62 (16.33)	6.88 (2.42)	5.24 (2.22)
A HD	0.24 (0.068)	0.03 (0.034)	0.02 (0.041)
A SHD	96.0 (27.47)	12.0 (13.8)	8.0 (16.52)

* WE OMIT $\times 10^{-2}$ IN THE VALUE DUE TO SPACE CONSIDERATION.

Experiment 2. We compare our proposed method with two benchmark methods. Here, we consider vanilla gradient descent (GD) and “re-start time” method [Bonnet et al., 2021, 2022]. Details on these benchmarks can be found in Appendix B.3. We report similar metrics over 100 independent trials in Table 5. As we can see, for both cases, our proposed method outperforms benchmarks in terms of most evaluation metrics. In case 1, even though GD with proper stopping criterion achieves slightly better ℓ_1 estimation error (for β and A), its pattern recovery of A is not as good as our proposed method (its HD and SHD are larger).

Table 5: Comparison with benchmarks. The best results are highlighted.

CASE 1: SINGLE SEQUENCE WITH TIME HORIZON $T = 10000$.				
METHOD	TWO-PHASE METHOD	VANILLA GD	EARLY STOPPED GD	RE-START
β ERR.	.312 (.112)	.393 (.035)	.264 (.137)	.837 (.246)
μ ERR.	.0386 (.0252)	.0413 (.0317)	.0398 (.0281)	.239 (.102)
A ERR.	1.726 (0.785)	23.58 (7.93)	1.494 (0.731)	8.828 (1.213)
A HD	.0304 (.0416)	.1336 (0.118)	.0936 (.0926)	.3576 (.0459)
A SHD	0.76 (1.04)	3.37 (2.96)	2.34 (2.32)	8.98 (1.19)

CASE 2: MULTIPLE (100) SEQUENCES WITH TIME HORIZON $T = 500$.				
METHOD	TWO-PHASE METHOD	VANILLA GD	EARLY STOPPED GD	RE-START
β ERR.	.219 (.157)	.377 (.058)	.286 (.120)	—
μ ERR.	.0367 (.0235)	.0335 (.0216)	.0363 (.0251)	—
A ERR.	.820 (.369)	21.350 (7.386)	1.551 (.577)	—
A HD	.0124 (.0231)	.105 (.120)	.0660 (.0687)	—
A SHD	.31 (.58)	2.64 (3.06)	1.65 (1.72)	—

We defer detailed experiment settings and additional results to Appendices B.1 and B.2.

5 Real data experiment

We created a retrospective cohort of patients utilizing in hospital data derived from rady hospital system in Atalanta, GA spanning 2018-2019. This data was collected and analyzed in accordance with Emory Institutional Review Board (IRB) approved protocol #STUDY00000302. Patients were included in the Sepsis-3 cohort if they met Sepsis-3 criteria while in the hospital and were admitted for ≥ 24 hours. Patients were included in the Non-Septic cohort if they had a SOFA score ≥ 2 . A total of 37 patient features comprised of laboratory results (labs) and observations (vital signs) were examined for this work. Treatments were limited to two classes of medication: antimicrobial therapy (e.g., antibiotics) and vasopressor therapy. We defer further details of the patient cohort construction to Appendix C.1. Here, we report the resulting descriptive statistics in Table 6.

Table 6: Median and interquartile range (IQR) of patients demographics.

YEAR	SEPSIS-3 PATIENTS		NON-SEPTIC PATIENTS	
	2018 ($n = 409$) *	2019 ($n = 454$)	2018 ($n = 960$)	2019 ($n = 1169$)
AGE (MEDIAN AND IQR)	58 (38 - 68)	59 (46 - 68)	56 (38 - 67)	55 (37 - 66)
FEMALE (PERCENTAGE)	30.1 %	36.6 %	37.1 %	35.8 %
AVERAGE SOFA SCORE	3.32	3.14	2.18	2.28
TRAJ. LEN. (MEDIAN)	25 (25 - 25)	25 (25 - 25)	17 (13 - 22)	17 (13 - 22)

* n REPRESENTS THE TOTAL NUMBER OF PATIENTS IN THE CORRESPONDING COHORT.

Integrating high-dimensional information (via, e.g., clustering) is essential in causal discovery and explainable machine learning [Sanchez et al., 2022]; examples include Uleman et al. [2021], Braman et al. [2021], Wei et al. [2021a]. While the Sepsis-3 definition provides the explicit features necessary for identifying the presence of sepsis, there is no consensus as to which features are best for prognosticating the disease. To reduce the complexity of our computations expert medical opinion was utilized to identify common and clinically relevant Sepsis-Associated Derangements (SADs) that could be detected using structured EMR data. A total of 18 SADs and 2 relevant treatments shown in Table 7 were identified using 37 patient features and treatments gathered from the medical record. A SAD was considered present if the patient features were outside of normal limits. Details on how SADs were constructed based on vital signs and labs can be found in Table 10 in Appendix C.1.

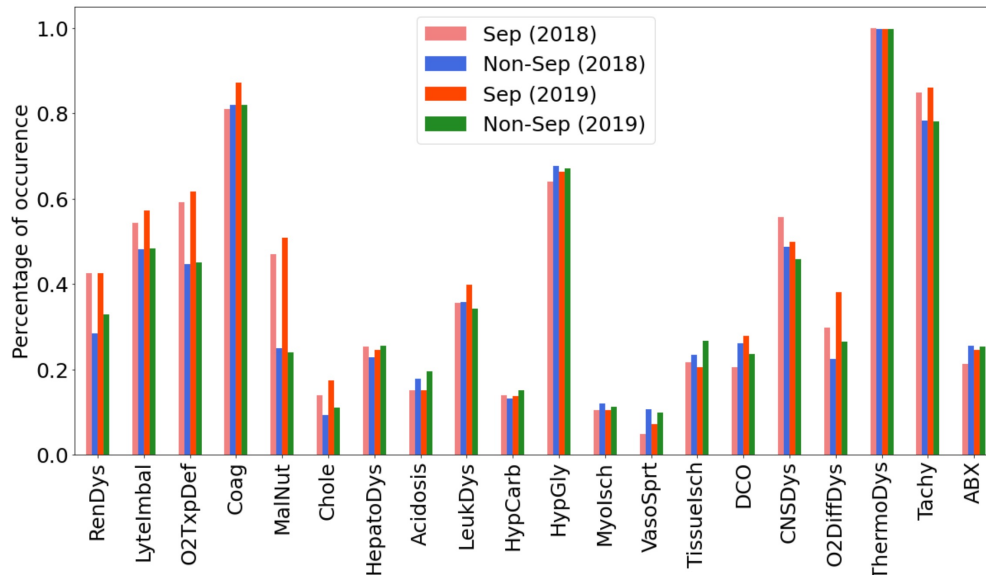


Figure 3: Percentage of SAD’s occurrence. Most SADs’ occurrences are more frequent in Sepsis-3 cohort.

Sepsis often shares symptoms with other disease processes making discrimination challenging.

Table 7: Measurements in sepsis-associated events construction.

SEPSIS-ASSOCIATED DERANGEMENT (SAD)		
FULL NAME	ABBREVIATION	MEASUREMENT NAME
RENAL DYSFUNCTION	RENDYS	CREATININE, BLOOD_UREA_NITROGEN_(BUN)
ELECTROLYTE IMBALANCE	LYTEIMBAL	CALCIUM, CHLORIDE, MAGNESIUM, POTASSIUM, PHOSPHORUS
OXYGEN TRANSPORT DEFICIENCY	O2TxPDEF	HEMOGLOBIN
COAGULOPATHY	COAG	PARTIAL_PROTHROMBIN_TIME_(PTT), FIBRINOGEN, PLATELETS, D_DIMER, THROMBIN_TIME, PROTHROMBIN_TIME_(PT), INR
MALNUTRITION	MALNUT	TRANSFERRIN, PREALBUMIN, ALBUMIN
CHOLESTASIS	CHOLE	BILIRUBIN_DIRECT, BILIRUBIN_TOTAL
HEPATOCELLULAR INJURY	HEPATOdYS	ASPARTATE_AMINOTRANSFERASE_(AST), AMMONIA, ALANINE_AMINOTRANSFERASE_(ALT)
ACIDOSIS	ACIDOSIS	BASE_EXCESS, PH
LEUKOCYTE DYSFUNCTION	LEUKDYS	WHITE_BLOOD_CELL_COUNT
HYPERCARBIA	HYPCARB	PARTIAL_PRESSURE_OF_CARBON_DIOXIDE_(PACO2), END_TIDAL_CO2
HYPERGLYCEMIA	HYPGLY	GLUCOSE
MYCARDIAL ISCHEMIA	MYOISCH	TROPONIN
TISSUE ISCHEMIA	TISSUEISCH	BASE_EXCESS, LACTIC_ACID
DIMINISHED CARDIAC OUTPUT	DCO	BEST_MAP
CNS DYSFUNCTION	CNSDys	GCS_TOTAL_SCORE
OXYGEN DIFFUSION DYSFUNCTION	O2DIFFDYS	SPO2, FIO2
THERMOREGULATION DYSFUNCTION	THERMODYS	TEMPERATURE
TACHYCARDIA	TACHY	PULSE

OTHER SEPSIS-ASSOCIATED EVENTS		
FULL NAME	ABBREVIATION	MEASUREMENT NAME
VASOPRESSOR SUPPORT	VASOSPRT	NOREPINEPHRINE_DOSE_WEIGHT, EPINEPHRINE_DOSE_WEIGHT, DOBUTAMINE_DOSE_WEIGHT, DOPAMINE_DOSE_WEIGHT, PHENYLEPHRINE_DOSE_WEIGHT, VASOPRESSIN_DOSE_WEIGHT
ANTIBIOTIC THERAPY	ABX	–
SEPSIS	SEP3	–

To evaluate the appropriateness of the constructed SADs the percentage of SAD occurrence (within the selected time window) was calculated for both septic and non-septic patients and can be seen for both years in Figure 3. It is expected that SADs would be present in both cohorts; however, the Sepsis-3 cohort demonstrated patterns showing a closer relationship with the SADs than the Non-Septic cohort.

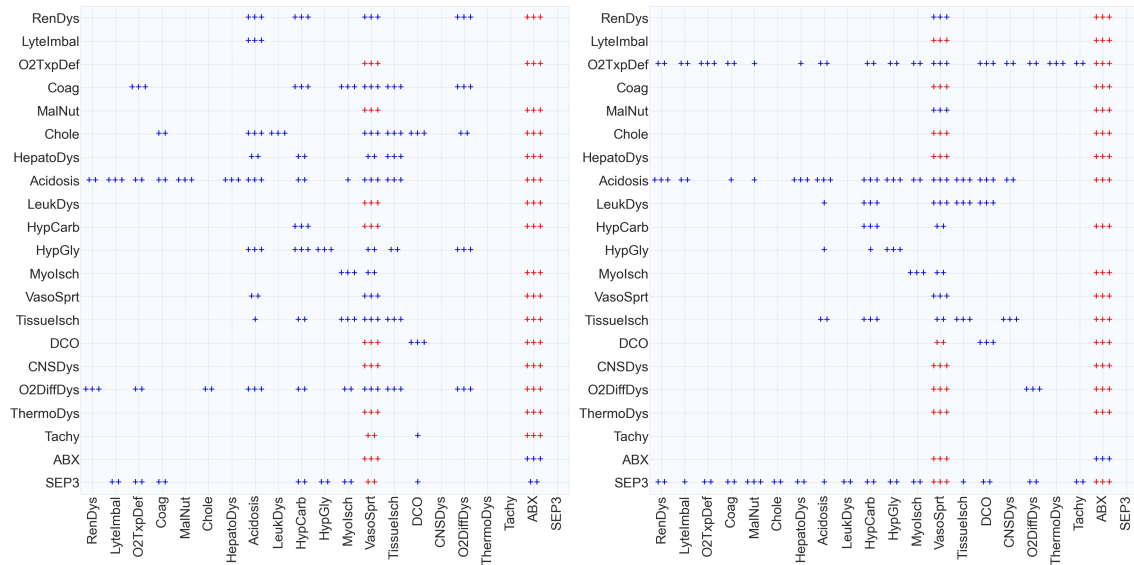


Figure 4: Adjacency matrices of the Granger Causal graphs for Sepsis-3 (left) and full (right) patient cohorts in Figure 1. “+”, “++” and “+++” correspond to the (absolute) value in $(0, .0005)$, $[.0005, .001)$ and $[.001, \infty)$, respectively, where the original values in the adjacency matrices are reported in Figures 9 and 10 in the Appendix. Nodes (i.e., SADs or SAEs) named along the X-axis can have either an inhibitory (red) or promoting effect (blue) on the nodes named in the Y-axis.

Recovering the GC graph. To study the temporal interactions between SADs (and other SAEs), we fit two GC graphs — one graph is on Sepsis-3 cohort and the other is on full patient cohort (i.e., the Sepsis-3 and Non-Septic cohorts combined). We report the results in Figure 4 and defer the training details to Appendix C.2. Both graphs demonstrate examples of clinically reasonable interactions between individual SADs (i.e., Oxygen Diffusion Dysfunction promotes Renal Dysfunction in the Septic cohort) and between SADs and Sepsis (i.e., Diminished Cardiac Output promotes Sepsis in both graphs). Interestingly the graph examining only the Sepsis-3 cohort identified more interactions between SADs than the one for the full patient cohort whereas the graph for the full patient cohort presented a higher number of strong relationships between SADs and sepsis suggesting that a time dependent, causal relationship exists between individual SADs and sepsis. A key finding across both graphs was the inhibitory effect of antibiotics on most SADs, which is consistent with the known ability of antibiotics to reduce in hospital mortality in sepsis patients [Seymour et al., 2017] presumably through preventing organ dysfunction like those identified via SADs.

While most of the relationships identified in these graphs are expected or feasible, vassopressors appear to unexpectedly inhibit both sepsis and the administration of antibiotics. In year 2018, among 409 (960) selected septic (non-septic) patients, there were 15 (96) who receive vasopressor support and 84 (231) who received antibiotics during the window, and only 3 (38) who received both vassopressors and antibiotics. This low number of vassopressor patients in the Sepsis-3 cohort is not unexpected as the time window for analysis is 24 hours prior to meeting the Sepsis-3 definition when most patients are not severely ill (see Appendix C.1 for more details). Additionally, antibiotics are dosed on scheduled intervals (e.g., once every six hours) whereas vassopressors are administered in a continuous fashion. These two attributes of the data set create a number of instances where vassopressors are administered without a formal antibiotic administration event in the following hour (though the patient may be on antibiotics). Additionally, each patient in the Sepsis-3 cohort is right censored after sepsis which means there is only one hour where the sepsis label is positive. Taken together these attributes of the data set likely explain why this unexpected relationship is seen.

Identifying the GC chain. The recovered GC graphs help reduce the problem of enumerating combinatorially many possible chains to finding the chains that only exist in the Sepsis-3 graph. However, even for a 2-by-2 sub-adjacency matrix, there could be multiple potential chain interpretations. We validate whether or not the chain structure reflects a unique pattern in Sepsis-3 cohort by performing Fisher's exact test and report the p -value. Here, we only focus on “++” and “+++” exciting effect when forming all possible chains. This method allows chains to be ranked in order of significance, affording those with domain expertise an efficient mechanism to inspect results. We report the top GC chains which are unique in the Sepsis-3 cohort for years 2018 (in-sample test) and 2019 (out-of-sample test) in Table 8. More details on those chains (including how to perform the test) and more identified chains can be found in Appendix C.3.

In Table 8, the chains possess a statistically strong relationship with patients in the Sepsis-3 cohort and correlate with clinical patterns that are often seen in sepsis. For example, Oxygen Diffusion Dysfunction (i.e., low oxygen saturation in the blood) is found to promote Renal Dysfunction and subsequent Oxygen Diffusion Dysfunction. Though not reflected in this table, septic patients could experience multiple chains simultaneously in addition to experiencing other discrete SADs simultaneous to events in a chain. This method to select and rank chains affords clinicians the ability to efficiently discover or follow those temporal patterns that differentiate septic patients from those experiencing organ injury caused by other diseases.

Table 8: Granger causal chains which are significantly unique in Sepsis-3 cohort in both years 2018 and 2019.

CHAIN:	TISSUEISCH	→	O2DIFFDYS	
P-VAL:	0.004 (2018)		0.092 (2019)	
CHAIN:	O2DIFFDYS	→	RENDYS	→ O2DIFFDYS
P-VAL:	0.107 (2018)		0.004 (2019)	
CHAIN:	VASOSPRT	→	TISSUEISCH	→ HEPATODYS
P-VAL:	0.052 (2018)		0.088 (2019)	
CHAIN:	LYTEIMBAL	→	ACIDOSIS	→ O2DIFFDYS
P-VAL:	0.009 (2018)		0.088 (2019)	
CHAIN:	ACIDOSIS	→	O2DIFFDYS	→ HYPGLY
P-VAL:	0.039 (2018)		0.063 (2019)	

6 Discussion

To conclude this paper, we briefly summarize the contribution and limitations of current work in this section. Our proposed method for Granger causal chain discovery provides a novel and scalable way to leverage clinical expertise to elucidate patterns of interest amongst large amounts of related EMR data. Though we do not build or validate a clinical alarm, this is very useful and logical extension of this work. Additionally, knowledge from the GC chains could be used to estimate risk of a future SAD (e.g., Renal Dysfunction) which might prompt a clinician to alter treatment (e.g., modify IV fluids therapy). A limitation of this work stems from the grouped nature of many lab results and vital sign measurements. It is not uncommon for multiple patient features to be recorded in the EMR with identical timestamps which means that multiple SADs can occur simultaneously. This presents challenges to our point process model which can not capture relationships between simultaneously occurring SADs. This could be remedied by incorporating second or third order interaction effect in ANOVA into the work to evaluate the effect of combined SADS on future patient states.

Another limitation of the method arises from the way treatments are administered. Some treatments (i.e., antibiotics) are dosed on an interval whereas others (i.e., vasopressors) are dosed continuously. This results in a higher number of “vasopressor” events than antibiotic events for certain patients and can lead to the false conclusion that vasopressors are inhibiting antibiotics which is not an expected finding. Future solutions could include representing antibiotics as a continuous medication similar to vasopressors so that the continuous effects of antibiotics are appreciated by the model.

From a modelling perspective an obvious drawback of Granger Causality is pointed out by Eichler and Didelez [2010], namely that A Granger-causes B does not imply that intervening in A would affect (the distribution on) B . A famous example is that the purchase of Christmas trees Granger-causes Christmas but this is clearly not the case. Another example is that disease B will lead to symptom A , say fever. Typically a person will first observe A and after diagnostic testing be diagnosed with B . Therefore, we should expect A Granger-caused B ; however, we should not expect that taking fever reducing medication (e.g., Tylenol), will help cure disease B (though it will alter the value of A).

This issue could be fixed in two possible ways: First, we should NOT treat the observed time as the exact event occurrence time. Instead, the exact occurrence time could be earlier than this observed time. By incorporating this time uncertainty, perhaps we can infer the true causal structure. Second, we can try to conduct counterfactual analysis by sampling counterfactual trajectories. This might be a direct application of Noorbakhsh and Rodriguez [2021], though we may need to extend this work to multivariate setting.

Moreover, our simple linear MHP fails to perform the sequential prediction task. This could be explained by the over-simplification of our model: on one hand, the dynamics within human body is too complex to be captured by simple linear relationship; on the other hand, exponential decaying kernel is problematic since an abnormal lab test result or vital sign for a small time period is “acceptable” whereas prolonged abnormality/dysfunction could lead to severe problem. Therefore, properly choosing the decaying kernel is very important. Nevertheless, since (1) it is easy to develop a scalable method to fit a simple model and (2) we do demonstrate its usefulness in identifying unique chain pattern in a real data experiment, we believe this is still a meaningful contribution to literature. Future work on how to utilize such chain patterns to perform sequential prediction, or how to use more complex yet explainable models (e.g., Wei et al. [2021a]) to fulfill such prediction purpose, needs to be done.

Lastly, from the optimization perspective, we only give a heuristic, i.e., our proposed two-phase algorithm, that works well in practice. Reformulating the problem via Lagrangian duality and using projected gradient descent to solve the dual problem could both work well in practice and enjoy strong convergence guarantee in theory. To be precise, the expansive projection for primal variables onto feasible region Θ (4) is reduced to the simple projection for dual variables onto $\mathbb{R}_+^{d \times d}$. Moreover, it is also worthwhile (numerically) explore the effect of other structures/regularizations on adjacency matrix, e.g., DAG structure [Zheng et al., 2018, Ng et al., 2020] or low-rank structure [Fang et al., 2020].

References

- Emmanuel Bacry, Iacopo Mastromatteo, and Jean-François Muzy. Hawkes processes in finance. *Market Microstructure and Liquidity*, 1(01):1550005, 2015.
- Yujia Bao, Zhaobin Kuang, Peggy Peissig, David Page, and Rebecca Willett. Hawkes process modeling of adverse drug reactions with longitudinal observational data. In *Machine learning for healthcare conference*, pages 177–190. PMLR, 2017.
- Sumanta Basu, Ali Shojaie, and George Michailidis. Network granger causality with inherent grouping structure. *The Journal of Machine Learning Research*, 16(1):417–453, 2015.
- Sumanta Basu, Xianqi Li, and George Michailidis. Low rank and structured modeling of high-dimensional vector autoregressions. *IEEE Transactions on Signal Processing*, 67(5):1207–1222, 2019.
- Andrew Bolstad, Barry D Van Veen, and Robert Nowak. Causal network inference via group sparse regularization. *IEEE transactions on signal processing*, 59(6):2628–2641, 2011.
- Anna Bonnet, Miguel Martinez Herrera, and Maxime Sangnier. Maximum likelihood estimation for hawkes processes with self-excitation or inhibition. *Statistics & Probability Letters*, 179:109214, 2021.
- Anna Bonnet, Miguel Martinez Herrera, and Maxime Sangnier. Inference of multivariate exponential hawkes processes with inhibition and application to neuronal activity. *arXiv preprint arXiv:2205.04107*, 2022.
- Nathaniel Braman, Jacob WH Gordon, Emery T Goossens, Caleb Willis, Martin C Stumpe, and Jagadish Venkataraman. Deep orthogonal fusion: Multimodal prognostic biomarker discovery integrating radiology, pathology, genomic, and clinical data. In *International Conference on Medical Image Computing and Computer-Assisted Intervention*, pages 667–677. Springer, 2021.
- Álvaro Cartea, Samuel N Cohen, and Saad Labyad. Gradient-based estimation of linear hawkes processes with general kernels. *arXiv preprint arXiv:2111.10637*, 2021.
- Wei Chen, Jibin Chen, Ruichu Cai, Yuequn Liu, and Zhifeng Hao. Learning granger causality for non-stationary hawkes processes. *Neurocomputing*, 468:22–32, 2022.

- Edward Choi, Nan Du, Robert Chen, Le Song, and Jimeng Sun. Constructing disease network and temporal progression model via context-sensitive hawkes process. In *2015 IEEE International Conference on Data Mining*, pages 721–726. IEEE, 2015.
- Michael Eichler and Vanessa Didelez. On granger causality and the effect of interventions in time series. *Lifetime data analysis*, 16(1):3–32, 2010.
- Michael Eichler, Rainer Dahlhaus, and Johannes Dueck. Graphical modeling for multivariate hawkes processes with nonparametric link functions. *Journal of Time Series Analysis*, 38(2): 225–242, 2017.
- Jalal Etesami, Negar Kiyavash, Kun Zhang, and Kushagra Singhal. Learning network of multivariate hawkes processes: A time series approach. *arXiv preprint arXiv:1603.04319*, 2016.
- Zhuangyan Fang, Shengyu Zhu, Jiji Zhang, Yue Liu, Zhitang Chen, and Yangbo He. Low rank directed acyclic graphs and causal structure learning. *arXiv preprint arXiv:2006.05691*, 2020.
- Lucas M Fleuren, Thomas LT Klausch, Charlotte L Zwager, Linda J Schoonmade, Tingjie Guo, Luca F Roggeveen, Eleonora L Swart, Armand RJ Girbes, Patrick Thorat, Ari Ercole, et al. Machine learning for the prediction of sepsis: a systematic review and meta-analysis of diagnostic test accuracy. *Intensive care medicine*, 46(3):383–400, 2020.
- Eric Warren Fox, Frederic Paik Schoenberg, and Joshua Seth Gordon. Spatially inhomogeneous background rate estimators and uncertainty quantification for nonparametric hawkes point process models of earthquake occurrences. *The Annals of Applied Statistics*, 10(3):1725–1756, 2016.
- Clive WJ Granger. Investigating causal relations by econometric models and cross-spectral methods. *Econometrica: journal of the Econometric Society*, pages 424–438, 1969.
- Clive WJ Granger. Testing for causality: a personal viewpoint. *Journal of Economic Dynamics and control*, 2:329–352, 1980.
- Clive WJ Granger. Some recent development in a concept of causality. *Journal of econometrics*, 39 (1-2):199–211, 1988.
- Alan G Hawkes. Point spectra of some mutually exciting point processes. *Journal of the Royal Statistical Society: Series B (Methodological)*, 33(3):438–443, 1971a.
- Alan G Hawkes. Spectra of some self-exciting and mutually exciting point processes. *Biometrika*, 58(1):83–90, 1971b.

- Alan G Hawkes and David Oakes. A cluster process representation of a self-exciting process. *Journal of Applied Probability*, 11(3):493–503, 1974.
- Tsuyoshi Ide, Georgios Kollias, Dzung Phan, and Naoki Abe. Cardinality-regularized hawkes-granger model. *Advances in Neural Information Processing Systems*, 34, 2021.
- Anatoli Juditsky, Arkadi Nemirovski, Liyan Xie, and Yao Xie. Convex parameter recovery for interacting marked processes. *IEEE Journal on Selected Areas in Information Theory*, 2020.
- Anatoli B Juditsky and AS Nemirovski. Signal recovery by stochastic optimization. *Automation and Remote Control*, 80(10):1878–1893, 2019.
- Diviyani Kalainathan and Olivier Goudet. Causal discovery toolbox: Uncover causal relationships in python. *arXiv preprint arXiv:1903.02278*, 2019.
- Sanggyun Kim, David Putrino, Soumya Ghosh, and Emery N Brown. A granger causality measure for point process models of ensemble neural spiking activity. *PLoS computational biology*, 7(3): e1001110, 2011.
- PA W Lewis and Gerald S Shedler. Simulation of nonhomogeneous poisson processes by thinning. *Naval research logistics quarterly*, 26(3):403–413, 1979.
- David Marsan and Olivier Lengline. Extending earthquakes’ reach through cascading. *Science*, 319 (5866):1076–1079, 2008.
- Hongyuan Mei and Jason M Eisner. The neural hawkes process: A neurally self-modulating multivariate point process. In *Advances in Neural Information Processing Systems*, pages 6754–6764, 2017.
- Sebastian Meyer and Leonhard Held. Power-law models for infectious disease spread. *The Annals of Applied Statistics*, 8(3):1612–1639, 2014.
- Ignavier Ng, AmirEmad Ghassami, and Kun Zhang. On the role of sparsity and dag constraints for learning linear dags. *Advances in Neural Information Processing Systems*, 33:17943–17954, 2020.
- Kimia Noorbakhsh and Manuel Gomez Rodriguez. Counterfactual temporal point processes. *arXiv preprint arXiv:2111.07603*, 2021.

- Christopher J Quinn, Negar Kiyavash, and Todd P Coleman. Equivalence between minimal generative model graphs and directed information graphs. In *2011 IEEE International Symposium on Information Theory Proceedings*, pages 293–297. IEEE, 2011.
- Matthew A Reyna, Chris Josef, Salman Seyedi, Russell Jeter, Supreeth P Shashikumar, M Brandon Westover, Ashish Sharma, Shamim Nemati, and Gari D Clifford. Early prediction of sepsis from clinical data: the physionet/computing in cardiology challenge 2019. In *2019 Computing in Cardiology (CinC)*, pages Page–1. IEEE, 2019.
- Pedro Sanchez, Jeremy P Voisey, Tian Xia, Hannah I Watson, Alison Q O’Neil, and Sotirios A Tsaftaris. Causal machine learning for healthcare and precision medicine. *Royal Society Open Science*, 9(8):220638, 2022.
- Frederic Paik Schoenberg, Marc Hoffmann, and Ryan J Harrigan. A recursive point process model for infectious diseases. *Annals of the Institute of Statistical Mathematics*, 71(5):1271–1287, 2019.
- Christopher W. Seymour, Foster Gesten, Hallie C. Prescott, Marcus E. Friedrich, Theodore J. Iwashyna, Gary S. Phillips, Stanley Lemeshow, Tiffany Osborn, Kathleen M. Terry, and Mitchell M. Levy. Time to Treatment and Mortality during Mandated Emergency Care for Sepsis. *N. Engl. J. Med.*, 376(23):2235–2244, 2017. ISSN 1533-4406. doi: 10.1056/NEJMoa1703058.
- Supreeth P. Shashikumar, Christopher S. Josef, Ashish Sharma, and Shamim Nemati. DeepAISE – An interpretable and recurrent neural survival model for early prediction of sepsis. *Artificial Intelligence in Medicine*, 113:102036, March 2021. ISSN 0933-3657. doi: 10.1016/j.artmed.2021.102036. URL <https://www.sciencedirect.com/science/article/pii/S0933365721000294>.
- Ali Shojaie and Emily B Fox. Granger causality: A review and recent advances. *arXiv preprint arXiv:2105.02675*, 2021.
- Vikas Sindhwani, Minh Ha Quang, and Aurélie C Lozano. Scalable matrix-valued kernel learning for high-dimensional nonlinear multivariate regression and granger causality. *arXiv preprint arXiv:1210.4792*, 2012.
- Mervyn Singer, Clifford S Deutschman, Christopher Warren Seymour, Manu Shankar-Hari, Djillali Annane, Michael Bauer, Rinaldo Bellomo, Gordon R Bernard, Jean-Daniel Chiche, Craig M Coopersmith, et al. The third international consensus definitions for sepsis and septic shock (sepsis-3). *Jama*, 315(8):801–810, 2016.

- Alex Tank, Ian Covert, Nicholas Foti, Ali Shojaie, and Emily Fox. Neural granger causality for nonlinear time series. *stat*, 1050:16, 2018.
- Jeroen F Uleman, René JF Melis, Rick Quax, Eddy A van der Zee, Dick Thijssen, Martin Dresler, Ondine van de Rest, Isabelle F van der Velpen, Hieab HH Adams, Ben Schmand, et al. Mapping the multicausality of alzheimer’s disease through group model building. *GeroScience*, 43(2): 829–843, 2021.
- Haoyun Wang, Liyan Xie, Alex Cuzzo, Simon Mak, and Yao Xie. Uncertainty quantification for inferring hawkes networks. *arXiv preprint arXiv:2006.07506*, 2020.
- Song Wei, Yao Xie, Christopher S Josef, and Rishikesan Kamaleswaran. Inferring granger causality from irregularly sampled time series. *arXiv preprint arXiv:2106.02600*, 2021a.
- Song Wei, Yao Xie, and Dobromir Rahnev. Inferring serial correlation with dynamic backgrounds. *arXiv preprint arXiv:2101.10962*, 2021b.
- WHO. Global report on the epidemiology and burden of sepsis: current evidence, identifying gaps and future directions. 2020.
- Hongteng Xu, Mehrdad Farajtabar, and Hongyuan Zha. Learning granger causality for hawkes processes. In *International Conference on Machine Learning*, pages 1717–1726. PMLR, 2016.
- Wei Zhang, Thomas Panum, Somesh Jha, Prasad Chalasani, and David Page. Cause: Learning granger causality from event sequences using attribution methods. In *International Conference on Machine Learning*, pages 11235–11245. PMLR, 2020.
- Xun Zheng, Bryon Aragam, Pradeep Ravikumar, and Eric P Xing. Dags with no tears: Continuous optimization for structure learning. *arXiv preprint arXiv:1803.01422*, 2018.
- Ke Zhou, Hongyuan Zha, and Le Song. Learning social infectivity in sparse low-rank networks using multi-dimensional hawkes processes. In *Artificial Intelligence and Statistics*, pages 641–649. PMLR, 2013.
- Jiancang Zhuang, Yosihiko Ogata, and David Vere-Jones. Stochastic declustering of space-time earthquake occurrences. *Journal of the American Statistical Association*, 97(458):369–380, 2002.
- Simiao Zuo, Haoming Jiang, Zichong Li, Tuo Zhao, and Hongyuan Zha. Transformer hawkes process. In *International conference on machine learning*, pages 11692–11702. PMLR, 2020.

A Additional details for our proposed algorithm

In the first phase, we perform projected GD. Instead of projecting back to the feasible region, we simply set all negative entries to zeros (which is a subset of the feasible region Θ (4)). Thus, this phase is computational friendly and can easily converge (to a neighborhood of the optimizer). Complete details of this phase can be found the in the following Algorithm 1.

Algorithm 1 Phase 1: Projected Gradient Descent.

Input: Data $(u_1, t_1), \dots, (u_N, t_N)$, learning rate γ_1 , stopping criterion (e.g., a certain number of iterations), decay parameter β_0

Initialization: Random initialize $\hat{\mu}_0$; Random or zero initialize \hat{A}_0 . Iteration index $t = 1$.

while stopping criterion NOT fulfilled **do**

1 Gradient Step: calculate the gradient

$$\nabla_{\mu} \tilde{\ell} = \nabla_{\mu} \tilde{\ell}(\hat{\mu}_{t-1}, \hat{A}_{t-1}; \beta_0), \quad \nabla_A \tilde{\ell} = \nabla_A \tilde{\ell}(\hat{\mu}_{t-1}, \hat{A}_{t-1}; \beta_0),$$

and then perform regular gradient descent with constant step length

$$\hat{\mu}_t \leftarrow \hat{\mu}_{t-1} + \gamma_1 \nabla_{\mu} \tilde{\ell} / \|\nabla_{\mu} \tilde{\ell}\|_2, \quad \hat{A}_t \leftarrow \hat{A}_{t-1} + \gamma_1 \nabla_A \tilde{\ell} / \|\nabla_A \tilde{\ell}\|_F.$$

2 Projection Step: project all negative entries of $\hat{\mu}_t$ and \hat{A}_t back to zeros

$$\hat{\mu}_t \leftarrow (\hat{\mu}_t)^+, \quad \hat{A}_t \leftarrow (\hat{A}_t)^+.$$

3 Update the iteration index $t \leftarrow t + 1$.

end while

Return: $\hat{\mu}_t, \hat{A}_t$.

After the initial phase, the iterate is in a neighborhood of the optimizer — we only need to further optimize those variables whose ground truth values are negative. To identify such variables, we use the gradient row vectors' ℓ_2 norms as the indicator — if the gradient's norm is large, the corresponding row vector in A may not converge. Complete details of this procedure are in Algorithm 2.

Algorithm 2 Phase 2: Locate the target indices for Batch Coordinate Gradient Descent.

Input: Data $(u_1, t_1), \dots, (u_N, t_N)$, decay parameter β_0 , a percentage threshold $p \in (0, 1)$ and the output of Phase 1 $(\hat{\mu}_0, \hat{A}_0)$ in Algorithm 1.

- Sort the index set $I = \{1, \dots, d\}$ such that the corresponding vector $\tilde{\ell}_2$ norm of the rows of the gradient matrix is in a descending order:

$$J = \{J_1, \dots, J_d\} = \arg \text{sort} \{ \|\nabla_{A_j} \tilde{\ell}(\hat{\mu}_0, \hat{A}_0; \beta_0)\|_2 : j \in I \},$$

where A_j denotes the j -th row of matrix A .

- Find the minimum number \tilde{d} of the first few indices in J such that the corresponding gradient row norms make up $p \times 100\%$ of the total F -norm of matrix A $\|\nabla_A \tilde{\ell}(\hat{\mu}_0, \hat{A}_0; \beta_0)\|_F$:

$$\tilde{d} = \arg \min \left\{ K : \sum_{k=1}^K \|\nabla_{A_{J_k}} \tilde{\ell}(\hat{\mu}_0, \hat{A}_0; \beta_0)\|_2^2 \geq p \|\nabla_A \tilde{\ell}(\hat{\mu}_0, \hat{A}_0; \beta_0)\|_F^2 \right\}$$

Return: J, \tilde{d} .

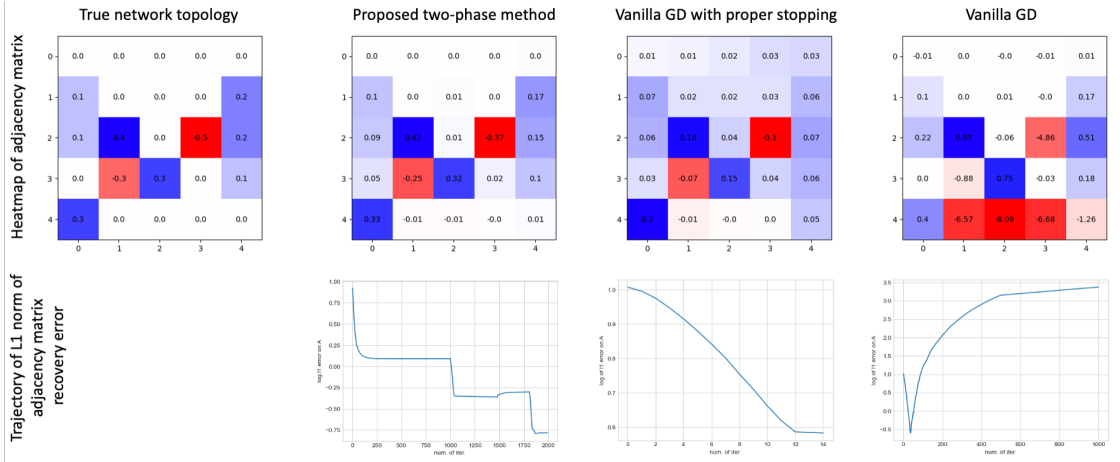


Figure 5: Comparison to GD via a $d = 5$ toy example. We can see (1) early stopped GD only converge to a very large neighborhood of the optimizer and (2) vanilla GD with fixed step size can easily diverge due to the existence of negative entries in the adjacency matrix.

Now, we are ready to perform batch coordinate descent for those selected variables. In this phase, we do not apply any projection to allow for possible negative iterates. However, similar to vanilla GD (as evidenced in Figure 5), the instability/divergence issue still exists. To handle such issue, we design a learning rate decaying scheme based on the gradient norm. Since the minimum of intensity becomes negative in phase 2, making the log-likelihood no longer well-defined (as shown in Figure 6), we propose to use gradient ℓ_2 norm to determine whether or not we should

decrease the learning rate in Phase 2. The intuition is simple: as we can see in Figure 6, due to the convexity of the objective function, we know the gradient should approach zero as we approach the global optimizer. We show the complete detail of the second part of phase 2 in Algorithm 3.

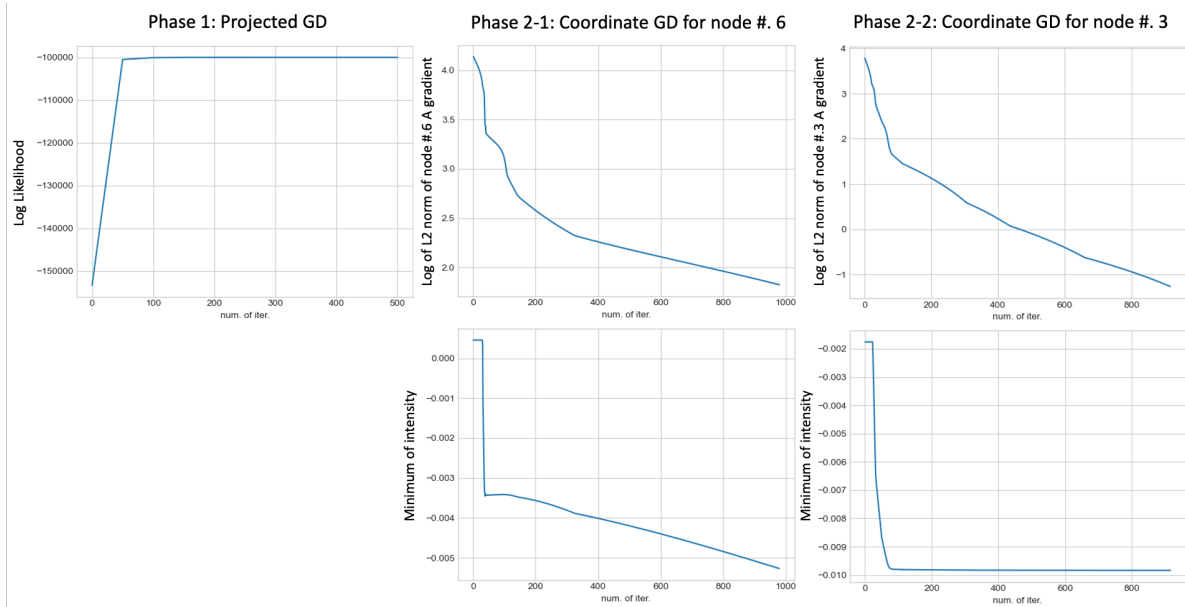


Figure 6: Demonstration of convergence for the $d = 10$ toy example in Figure 2. In phase 1, the log-likelihood gradually increase. In phase 2, the log-likelihood becomes intractable as the minimum of intensity (at even occurrence times) turns negative. Nevertheless, the decreasing gradient norm still shows the algorithm's convergence.

Algorithm 3 Phase 2: (Batch) Coordinate Descent for Selected variables.

Input: Data $(u_1, t_1), \dots, (u_N, t_N)$, learning rate γ_2 , decay parameter β_0 , a learning rate threshold γ_0 , target index set J , \tilde{d} from Algorithm 2 and the output of Phase 1 in Algorithm 1 $(\hat{\mu}_0, \hat{A}_0)$.

for $i = J_1, \dots, J_{\tilde{d}}$ **do**

Initialize iteration index $t = 1$ and learning rate $\tilde{\gamma}_2 = \gamma_2$.

while $\tilde{\gamma}_2 > \gamma_0$ **do**

1 Calculate the gradient

$$\nabla_{A_i} \tilde{\ell} = \nabla_{A_i} \tilde{\ell}(\hat{\mu}_0, \hat{A}_{t-1}; \beta_0),$$

and then perform regular gradient descent with constant step length

$$(\hat{A}_t)_i \leftarrow (\hat{A}_{t-1})_i + \tilde{\gamma}_2 \nabla_{A_i} \tilde{\ell} / \|\nabla_{A_i} \tilde{\ell}\|_2.$$

2 **if** $\|\nabla_{A_i} \tilde{\ell}\|_2 < \|\nabla_{A_i} \tilde{\ell}(\hat{\mu}_0, \hat{A}_t; \beta_0)\|_2$ **then**

Decrease learning rate $\tilde{\gamma}_2 \leftarrow \tilde{\gamma}_2/2$ and cancel the update $(\hat{A}_t)_i \leftarrow (\hat{A}_{t-1})_i$.

end if

3 Update the iteration index $t \leftarrow t + 1$.

end while

Update $(\hat{A}_0)_i \leftarrow (\hat{A}_t)_i$ and initialize iteration index $t = 1$ and learning rate $\tilde{\gamma}_2 = \gamma_2$.

while $\tilde{\gamma}_2 > \gamma_0$ **and** $(\hat{\mu}_{t-1})_i > 0$ **do**

1 Gradient Step: Calculate the gradient

$$\nabla_{\mu_i} \tilde{\ell} = \nabla_{\mu_i} \tilde{\ell}(\hat{\mu}_t, \hat{A}_0; \beta_0),$$

and then perform regular gradient descent with constant step length

$$(\hat{\mu}_t)_i \leftarrow (\hat{\mu}_{t-1})_i + \tilde{\gamma}_2 \nabla_{\mu_i} \tilde{\ell} / \|\nabla_{\mu_i} \tilde{\ell}\|_2.$$

2 Projection Step: $(\hat{\mu}_t)_i \leftarrow ((\hat{\mu}_t)_i)^+$.

3 **if** $\|\nabla_{\mu_i} \tilde{\ell}\|_2 < \|\nabla_{\mu_i} \tilde{\ell}(\hat{\mu}_t, \hat{A}_0; \beta_0)\|_2$ **then**

Decrease learning rate $\tilde{\gamma}_2 \leftarrow \tilde{\gamma}_2/2$ and cancel the update $(\hat{\mu}_t)_i \leftarrow (\hat{\mu}_{t-1})_i$.

end if

4 Update the iteration index $t \leftarrow t + 1$.

end while

Update $(\hat{\mu}_0)_i \leftarrow (\hat{\mu}_t)_i$.

end for

Return: $\hat{\mu}_0, \hat{A}_0$.

B Additional details for numerical simulation

B.1 Experimental details

Synthetic data generation. We use Lewis’ thinning algorithm [Lewis and Shedler, 1979] to simulate the multivariate Hawkes process data. In this experiment, we fix the decay parameter $\beta = 0.8$ and randomly initialize the background intensity vector $\mu \in \mathbb{R}^d$ and the network adjacency matrix $A \in \mathbb{R}^{d \times d}$. Each entry of μ (and A) is uniformly random number in $[0, 0.1]$ (and $[0, 0.4]$). Next, we apply vanilla GD to minimize function $h(A) = \text{tr}(e^A) - d$ to zero, in order to obtain a Directed acyclic graph (DAG) [Zheng et al., 2018]. Last but not least, we randomly assign random negative entries ($U([-0.5, 0])$) to A and round all entries of μ and A to one decimal place. Even though the synthetic data only considers DAG as input, we want to mention that we do not explicitly use the structure in the learning process. Most importantly, the ℓ_1 recover error is also reported, which can validate the effectiveness of our method for most type of random graphs.

Evaluation metrics. Here, we report the following metrics

- (1) absolute value of β recovery error;
- (2) vector ℓ_1 norm of μ recovery error;
- (3) vector ℓ_1 norm of A recovery error;
- (4) Hamming Distance between ground truth and fitted (after thresholding) adjacency matrix A ;
- (5) Structural Hamming Distance between ground truth and fitted (after thresholding) adjacency matrix A .

Note that metric (3) aims to evaluate how the fitted values deviate from the ground truth whereas metrics (4) and (5) aim to show how the recovered “pattern” resembles the ground truth. The Hamming Distance is defined to be the number of differences between the supports of ground truth and fitted (after thresholding) adjacency matrix A . For SHD, recall that it is defined as the total number of edge additions, deletions and reversals needed to convert the estimated DAG into the true DAG. Its evaluation is readily implemented in a python package `cdt` [Kalainathan and Goudet, 2019] and we refer readers to Appendix D.2 in Zheng et al. [2018] for a more detailed definition.

Last but not least, the hard thresholding of fitted adjacency matrix is done by zeroing out all entries whose absolute values are smaller than a threshold. We start with the smallest value of all absolute values of the non-zero entries in the fitted matrix as the threshold. We gradually increase this threshold until the resulting graph is a DAG (i.e., $h(A) = 0$).

B.2 Results

Since the log-likelihood is intractable in phase 2 coordinate descent, we also try the matrix Frobenius Norm (F -norm) of the gradient w.r.t. A as the GoF metric to select the (hyper-)parameter β . To be precise, we will select the β with smallest gradient (w.r.t. A) F -norm as the estimated decay parameter. We report the results in Table 9.

Table 9: Median and standard deviation of (1) ℓ_1 norm of μ recovery error (μ err.); (2) ℓ_1 norm of A recovery error (A err.); (3) Hamming Distance between ground truth and fitted adjacency matrix A (A HD); (4) Structural Hamming Distance between ground truth and fitted adjacency matrix A (A SHD). The last row corresponds to selected β by using matrix F -norm of phase-two A gradient as criterion, where we can observe its performance is not as good as what we have when we use phase-one log-likelihood as the criterion in Table 1.

β	$d = 5$				$d = 10$			
	μ ERR.*	A ERR.	A HD	A SHD	μ ERR.*	A ERR.	A HD	A SHD
0.4	4.14 (2.79)	1.34 (0.25)	0.08 (0.093)	2.0 (2.33)	8.6 (3.83)	4.37 (0.64)	0.04 (0.054)	4.0 (5.47)
0.5	4.27 (2.93)	1.11 (0.25)	0.08 (0.087)	2.0 (2.19)	10.49 (4.4)	3.49 (0.61)	0.02 (0.035)	2.0 (3.52)
0.6	4.26 (2.88)	0.86 (0.24)	0.04 (0.074)	1.0 (1.86)	9.84 (4.34)	2.58 (0.63)	0.02 (0.025)	2.0 (2.51)
0.7	3.78 (2.74)	0.63 (0.22)	0.02 (0.062)	0.5 (1.55)	8.68 (4.02)	1.87 (0.63)	0.01 (0.026)	1.0 (2.61)
0.8	3.57 (2.6)	0.54 (0.23)	0.0 (0.051)	0.0 (1.29)	7.33 (3.72)	1.4 (0.49)	0.01 (0.018)	1.0 (1.89)
0.9	3.53 (2.52)	0.64 (0.22)	0.0 (0.038)	0.0 (0.96)	6.46 (3.52)	1.53 (0.42)	0.01 (0.021)	1.0 (2.17)
1	3.79 (2.45)	0.91 (0.24)	0.0 (0.035)	0.0 (0.88)	7.09 (3.45)	1.84 (0.39)	0.01 (0.022)	1.0 (2.2)
1.1	3.68 (2.35)	1.14 (0.28)	0.0 (0.024)	0.0 (0.61)	7.61 (3.4)	2.3 (0.34)	0.02 (0.027)	2.0 (2.71)
1.2	3.85 (2.23)	1.31 (0.36)	0.0 (0.029)	0.0 (0.73)	8.05 (3.37)	2.71 (0.38)	0.03 (0.034)	3.0 (3.47)
–	4.04 (2.46)	0.98 (0.53)	0.0 (0.028)	0.0 (0.7)	7.47 (3.26)	2.34 (0.66)	0.02 (0.03)	2.0 (3.0)

* WE OMIT $\times 10^{-2}$ IN THE VALUE DUE TO SPACE CONSIDERATION.

We can see it does not perform well for $d = 10$ case, compared to using phase-one log-likelihood as the GoF metric. Last but not least, since we have phase-one log-likelihood as a valid GoF metric, we can apply ℓ_1 penalty in the MLE formulation (6) to impose sparse structure on graph structure A .

B.3 Benchmarks

Here, we give details on the benchmark methods that we compare with in our numerical simulation. For vanilla GD, we use fixed step size without any decaying scheme and for early stopped GD, we decrease the step size by half whenever the gradient norm increases (as the log-likelihood could be intractable). For the “re-start time” method, we only give a graphical illustration here and refer readers to Bonnet et al. [2021, 2022] for more details.

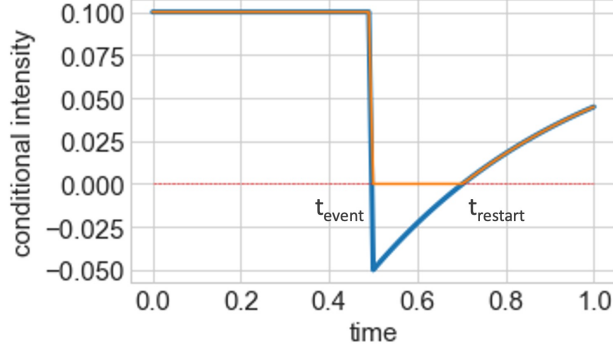


Figure 7: Illustration of re-start time [Bonnet et al., 2021].

As one can see in Figure 7, the orange line corresponds to the true conditional intensity $\lambda_i(t)$ (1) where as the blue line corresponds to the $\tilde{\lambda}_i(t)$ where we drop the $(\cdot)^+$ operator. To evaluate the log-likelihood, for each event occurrence time t_{event} we need to calculate a re-start time t_{restart} as shown in the above figure. Clearly, when we are faced with a multivariate problem, we need to calculate re-start time for ALL variables at each event occurrence time. Thus, this calculation is very computationally intensive and we did encounter such issue when performing our numerical simulation in $d = 20$ case. Moreover, the authors did not talk about how to generalize their method to multi-sequence case and therefore we did not compare with this method in multi-sequence case.

C Additional details for real data experiment

C.1 Data description and SAD construction

All patient data for each encounter was binned into hourly windows that began with hospital admission and ended with discharged. If more than one measurement occurred in an hour, then the mean of the values was recorded. To ensure that model training was performed on data series of similar lengths, a 24 hour subset of the full patient encounter was selected for analysis. For patients in the Sepsis-3 cohort the 24 hour window ended with when the patient met Sepsis-3 criteria (SEP3 time). For the Non-Septic cohort the window was centered (i.e., 12 hours before and after) upon the first time a patient had a SOFA score ≥ 2 (SOFA time). In some instances the event of interest (i.e., SOFA time or SEP3 time) occurred close to admission or discharge, resulting in a truncated data set of < 24 hours.

The raw features from EMR data we are using include: (1) *Vital Signs* - in ICU environments these are normally recorded at an hourly interval, however, patients on the floor may only have vital signs measured once every 8 hours. (2) *Lab Results* - These tests are most commonly collected

once every 24 hours; however, this collection frequency may change based on the severity of a patient’s illness. In this study, we include in total 6 vital signs and 31 labs. Those vital signs and labs are presented in the SAD construction table in Table 10 below. As those measurement names explain themselves, we do not give further description of the meaning of those measurements.

Table 10: SAD construction based on thresholding observed vital signs and Labs via medical knowledge. In our study, we incorporate in total 37 patient features, including 31 labs and 6 vital signs.

FULL NAME (ABBREV.)	TYPE	MEASUREMENT NAME	ABNORMAL THRESHOLD
RENAL DYSFUNCTION (RENDYS)	LAB	CREATININE	> 1.3
		BLOOD_UREA_NITROGEN_(BUN)	> 20
ELECTROLYTE IMBALANCE (LYTEIMBAL)	LAB	CALCIUM	> 10.5
		CHLORIDE	< 98 OR > 106
		MAGNESIUM	< 1.6
		POTASSIUM	> 5.0
		PHOSPHORUS	> 4.5
OXYGEN TRANSPORT DEFICIENCY (O2TXPDEF)	LAB	HEMOGLOBIN	< 12
COAGULOPATHY (COAG)	LAB	PARTIAL_PROTHROMBIN_TIME_(PTT)	> 35
		FIBRINOGEN	< 233
		PLATELETS	< 150000
		D_DIMER	> 0.5
		THROMBIN_TIME	> 20
		PROTHROMBIN_TIME_(PT)	> 13
		INR	> 1.5
MALNUTRITION (MALNUT)	LAB	TRANSFERRIN	< 0.16
		PREALBUMIN	< 16
		ALBUMIN	< 3.3
CHOLESTATSIS (CHOLE)	LAB	BILIRUBIN_DIRECT	> 0.3
		BILIRUBIN_TOTAL	> 1.0
HEPATOCELLULAR INJURY (HEPATO DYS)	LAB	ASPARTATE_AMINOTRANSFERASE_(AST)	> 40
		ALANINE_AMINOTRANSFERASE_(ALT)	> 40
		AMMONIA	> 70
ACIDOSIS (ACIDOSIS)	LAB	BASE_EXCESS	< -3
		PH	< 7.32
LEUKOCYTE DYSFUNCTION (LEUKDYS)	LAB	WHITE_BLOOD_CELL_COUNT	< 4 OR > 12
HYPERCARBIA (HYPCARB)	LAB	END_TIDAL_CO2	> 45
		PARTIAL_PRESSURE_OF_CARBOON_DIOXIDE_(PACO2)	> 45
HYPERGLYCEMIA (HYPGLY)	LAB	GLUCOSE	> 125
MYCARDIAL ISCHEMIA (MYOISCH)	LAB	TROPONIN	> 0.04
TISSUE ISCHEMIA (TISSUEISCH)	LAB	BASE_EXCESS	< -3
		LACTIC_ACID	> 2.0
DIMINISHED CARDIAC OUTPUT (DCO)	VITAL SIGNS	BEST_MAP	< 65
CNS DYSFUNCTION (CNSDYS)	VITAL SIGNS	GCS_TOTAL_SCORE	< 14
OXYGEN DIFFUSION DYSFUNCTION (O2DIFFDYS)	VITAL SIGNS	SPO2	< 92
		FIO2	> 21
THERMOREGULATION DYSFUNCTION (THERMODYS)	VITAL SIGNS	TEMPERATURE	< 36 OR > 38
TACHYCARDIA (TACHY)	VITAL SIGNS	PULSE	> 90

C.2 Granger Causal graph recovery

In our real data experiment, we additionally add ℓ_1 regularization to enforce sparse structure on fitted adjacency matrix, i.e., the estimate is obtained by solving the following optimization problem:

$$\hat{\mu}, \hat{A} = \operatorname{argmin}_{\mu, A \in \Theta} -\tilde{\ell}(\mu, A; \beta) + \lambda_1 \|A\|_1, \quad (7)$$

where $\tilde{\ell}(\mu, A; \beta)$ is the surrogate log-likelihood defined in (3). Here, both regularization parameter λ_1 and decaying rate parameter β are hyperparameters. We use grid-search to find their optimal values. To be precise, in our real data experiments, we search $\lambda_1 \in \{0.05, 0.1, 0.15, 0.2, 0.25, 0.3, 0.35, 0.4, 0.5\}$ and $\beta \in \{0.01, 0.015, 0.02, 0.025, 0.03, 0.035, 0.04\}$.

Most importantly, we also find that our algorithm is very sensitive to the phase 1 learning rate γ_1 choice. Thus, we also use end-of-phase 1 likelihood as the GoF criterion to select the best γ_1 . In phase 1, we run 1000 iterations and reduce the learning rate by half every 200 iterations. The trade-off is, choosing overly small learning rate cannot guarantee convergence within the limited iterations whereas overly large learning rate will lead to divergence or over-fitting. Here, when we train the model for Sepsis-3 cohort, we search $\gamma_1 \in \{0.6, 0.59, 0.58, 0.57, 0.56, 0.55, 0.54, 0.53, 0.52, 0.5, 0.48, 0.46, 0.4, 0.3, 0.2, 0.1\}$. For the full patient model, we search $\gamma_1 \in \{0.97, 0.96, 0.95, 0.9, 0.85, 0.8, 0.75, 0.7, 0.5, 0.49, 0.48, 0.47, 0.46, 0.4, 0.3, 0.2, 0.1\}$.

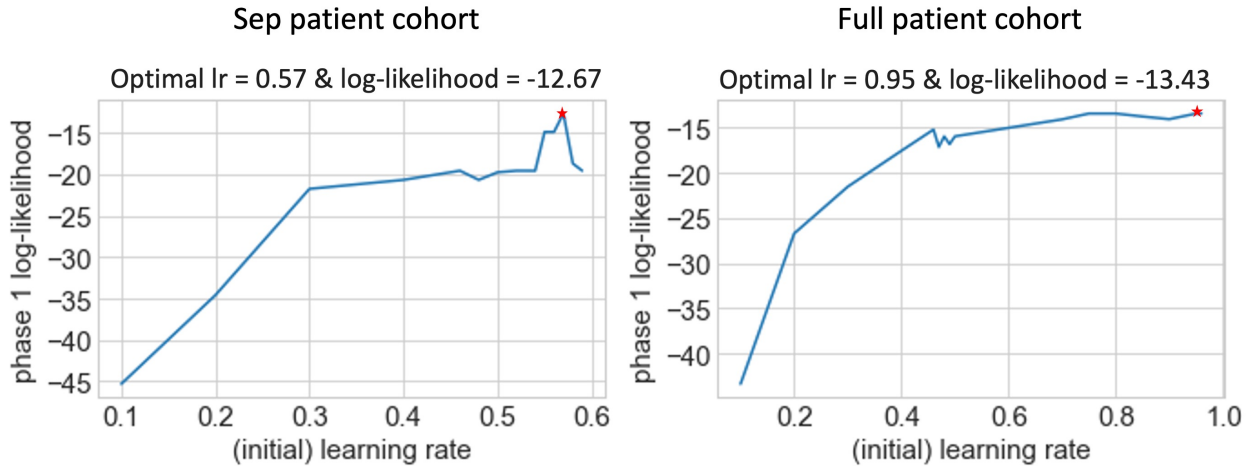


Figure 8: End-of-phase 1 log-likelihood versus learning rate. Each point on the curve corresponds to the optimal selected (λ_1, β) pair on our selected grid based on the end-of-phase 1 log-likelihood. We do not try larger γ_1 on full patient cohort due to divergence. The optimal learning rate is marked with red star and its value is on the top of the corresponding figure.

We fit the model using the data in year 2018. We report the end-of-phase 1 log-likelihood versus learning rate in Figure 8, where each point on the curve corresponds to the optimal selected (λ_1, β)

pair based on the end-of-phase 1 log-likelihood. For Sepsis-3 model, the optimal hyperparameters are: $\gamma_1 = 0.57$, $\lambda_1 = 0.25$, $\beta = 0.03$; for the full patient model, the optimal hyperparameters are: $\gamma_1 = 0.95$, $\lambda_1 = 0.5$, $\beta = 0.02$. We also want to mention that for $\gamma_1 \geq 0.97$, our algorithm diverges for full patient cohort and therefore we do not try larger γ_1 choices.

The background intensity for both models are: (1) For Sepsis-3 model, we have fitted background intensities are .0326, 0.0424, 0.0698 and 0.0363 for Electrolyte Imbalance, Thermoregulation Dysfunction, Tachycardia and Sepsis, respectively, whereas the rest of the SAEs’ background intensities are all zeros; (2) For full patient model, we have 0.0676, 0.0514, 0.0719 for Hyperglycemia, Thermoregulation Dysfunction, Tachycardia, respectively, and the rest are all zeros. Most importantly, the recovered mutual excitation and inhibition matrices are reported in Figures 9 and 10, respectively.

C.3 Granger Causal chain discovery and identification

Now, we are ready to identify the chain structures/patterns which are unique in Sepsis-3 cohort. However, those entries could correspond to chains with different orders and lengths. Therefore, we still need to use a more convincing method to validate the uniqueness of those possible chains in the Sepsis-3 GC graph (and not in the full patient GC graph).

Let us take a two-node graph as an example: for RenDys and O2DiffDys, we can extract a 2-by-2 sub-adjacency matrix in Sepsis-3 GC graph. As we can see, only the self-exciting effect is zero in this sub-matrix, leading to 2 possible length-2 chain structures: RenDys \rightarrow O2DiffDys and O2DiffDys \rightarrow RenDys, 3 possible length-3 chain structures: RenDys \rightarrow O2DiffDys \rightarrow O2DiffDys, O2DiffDys \rightarrow O2DiffDys \rightarrow RenDys and O2DiffDys \rightarrow RenDys \rightarrow O2DiffDys, and so on.

To identify which chain structure leads to the entries in the GC graph, we perform Fisher’s exact test, which is a powerful hypothesis testing tool on the equality of ratios between two groups when the sample size is relatively small. To be precise, given a chain structure, assume we observe the following table:

Table 11: Data for Fisher’s exact test

count	Sep	Non-Sep
with chain	a	b
without chain	c	d

The estimates of probabilities of such chain structure’s occurrence in both groups are given by

$$\hat{p}_{\text{sep}} = \frac{a}{a + c}, \quad \hat{p}_{\text{non-sep}} = \frac{b}{b + d}.$$

Under the null hypothesis $H_0 : p_{\text{sep}} = p_{\text{non-sep}}$, the probability of observing the above Table 11 is

$$p = \frac{\binom{a+b}{a} \binom{c+d}{c}}{\binom{n}{a+c}} = \frac{\binom{a+b}{b} \binom{c+d}{d}}{\binom{n}{b+d}} = \frac{(a+b)!(c+d)!(a+c)!(b+d)!}{a!b!c!d!n!},$$

where $n = a + b + c + d$. This is the p -value of Fisher's exact test and we will reject H_0 if this value is smaller than a chosen significance level α (e.g., 0.05 or 0.1).

In our real data experiment, for a given chain structure, we first extract data with all events in the chain to form Table 11, and then calculate a p -value based on the above formula. We choose $\alpha \approx 0.1$ as the significance level. We say a discovered chain (by our GC graphs) is identified to be (significantly) unique in Sepsis-3 cohort if the corresponding p -value of Fisher's exact test is smaller than our selected significance level α .

In the following, we will report the data table (as shown in Table 11), ratio estimates $\hat{p}_{\text{sep}}, \hat{p}_{\text{non-sep}}$ and the p -value for all significantly unique chains. We report the chains which are significantly unique in Sepsis-3 cohort in both year 2018 (i.e., in-sample test) and year 2019 (i.e., out-of-sample test) in Table 12. In addition, we also report the chains which are only significantly unique in Sepsis-3 cohort in one year in Tables 13 (year 2018) and 14 (year 2019).

Table 12: Chains which are significantly unique in Sepsis-3 cohort in both 2018 and 2019.

CHAIN:	TISSUEISCH	→	O2DIFFDYS			
			2018		2019	
			SEP	NON-SEP	SEP	NON-SEP
	COUNT		17	20	19	35
			5	30	6	28
	RATIO		0.772	0.4	0.76	0.555
	P-VAL		0.004		0.092	
CHAIN:	O2DIFFDYS	→	RENDYS		→	O2DIFFDYS
			2018		2019	
			SEP	NON-SEP	SEP	NON-SEP
	COUNT		35	31	49	33
			14	25	17	34
	RATIO		0.714	0.553	0.742	0.492
	P-VAL		0.107		0.004	
CHAIN:	VASOSPRT	→	TISSUEISCH		→	HEPATO DYS
			2018		2019	
			SEP	NON-SEP	SEP	NON-SEP
	COUNT		3	3	3	2
			1	14	3	15
	RATIO		0.75	0.176	0.5	0.117
	P-VAL		0.052		0.088	
CHAIN:	LYTEIMBAL	→	ACIDOSIS		→	O2DIFFDYS
			2018		2019	
			SEP	NON-SEP	SEP	NON-SEP
	COUNT		8	7	9	13
			2	17	3	19
	RATIO		0.8	0.291	0.75	0.406
	P-VAL		0.009		0.088	
CHAIN:	ACIDOSIS	→	O2DIFFDYS		→	HYPGLY
			2018		2019	
			SEP	NON-SEP	SEP	NON-SEP
	COUNT		6	13	9	13
			1	20	6	30
	RATIO		0.857	0.393	0.6	0.302
	P-VAL		0.039		0.063	

Table 13: Chains which are only significantly unique in Sepsis-3 cohort in year 2018.

CHAIN: MALNUT → ACIDOSIS					
	2018		2019		
	SEP	NON-SEP	SEP	NON-SEP	
COUNT	24	20	21	35	
	9	27	11	34	
RATIO	0.727	0.425	0.656	0.507	
P-VAL	0.011		0.198		
CHAIN: RENDYS → O2DIFFDYS					
	2018		2019		
	SEP	NON-SEP	SEP	NON-SEP	
COUNT	44	39	57	50	
	5	17	9	17	
RATIO	0.897	0.696	0.863	0.746	
P-VAL	0.015		0.125		
CHAIN: TISSUEISCH → O2DIFFDYS → HYPGLY					
	2018		2019		
	SEP	NON-SEP	SEP	NON-SEP	
COUNT	10	11	11	23	
	3	28	6	31	
RATIO	0.769	0.282	0.647	0.425	
P-VAL	0.003		0.164		
CHAIN: ACIDOSIS → RENDYS → O2DIFFDYS → HYPGLY					
	2018		2019		
	SEP	NON-SEP	SEP	NON-SEP	
COUNT	5	3	4	2	
	1	8	4	11	
RATIO	0.833	0.272	0.5	0.153	
P-VAL	0.049		0.146		
CHAIN: TISSUEISCH → O2DIFFDYS → RENDYS → O2DIFFDYS					
	2018		2019		
	SEP	NON-SEP	SEP	NON-SEP	
COUNT	7	2	6	7	
	5	19	4	17	
RATIO	0.583	0.095	0.6	0.291	
P-VAL	0.004		0.129		
CHAIN: ACIDOSIS → LYTEIMBAL → ACIDOSIS → O2DIFFDYS					
	2018		2019		
	SEP	NON-SEP	SEP	NON-SEP	
COUNT	5	4	6	7	
	5	20	6	25	
RATIO	0.5	0.166	0.5	0.218	
P-VAL	0.084		0.134		
CHAIN: LYTEIMBAL → ACIDOSIS → O2DIFFDYS → HYPGLY					
	2018		2019		
	SEP	NON-SEP	SEP	NON-SEP	
COUNT	4	4	6	7	
	2	17	5	22	
RATIO	0.666	0.19	0.545	0.241	
P-VAL	0.044		0.127		

Table 14: Chains which are NOT significantly unique in Sepsis-3 cohort in year 2018, but significantly unique in year 2019.

CHAIN: O2DIFFDYS → RENDYS					
	2018		2019		
	SEP	NON-SEP	SEP	NON-SEP	
COUNT	40	43	55	47	
	9	13	11	20	
RATIO	0.816	0.767	0.833	0.701	
P-VAL	0.633		0.1		
CHAIN: VASOSPRT → ACIDOSIS → RENDYS					
	2018		2019		
	SEP	NON-SEP	SEP	NON-SEP	
COUNT	2	7	4	3	
	1	9	2	13	
RATIO	0.666	0.437	0.666	0.187	
P-VAL	0.582		0.053		
CHAIN: RENDYS → O2DIFFDYS → RENDYS					
	2018		2019		
	SEP	NON-SEP	SEP	NON-SEP	
COUNT	32	31	47	35	
	17	25	19	32	
RATIO	0.653	0.553	0.712	0.522	
P-VAL	0.324		0.032		
CHAIN: VASOSPRT → TISSUEISCH → ACIDOSIS → RENDYS					
	2018		2019		
	SEP	NON-SEP	SEP	NON-SEP	
COUNT	2	7	3	0	
	1	7	3	15	
RATIO	0.666	0.5	0.5	0.0	
P-VAL	1.0		0.015		
CHAIN: O2DIFFDYS → RENDYS → O2DIFFDYS → RENDYS					
	2018		2019		
	SEP	NON-SEP	SEP	NON-SEP	
COUNT	32	31	48	31	
	17	25	18	36	
RATIO	0.653	0.553	0.727	0.462	
P-VAL	0.324		0.002		
CHAIN: RENDYS → O2DIFFDYS → RENDYS → O2DIFFDYS					
	2018		2019		
	SEP	NON-SEP	SEP	NON-SEP	
COUNT	31	31	46	34	
	18	25	20	33	
RATIO	0.632	0.553	0.696	0.507	
P-VAL	0.433		0.033		
CHAIN: O2DIFFDYS → RENDYS → O2DIFFDYS → COAG					
	2018		2019		
	SEP	NON-SEP	SEP	NON-SEP	
COUNT	28	26	40	25	
	17	20	20	33	
RATIO	0.622	0.565	0.666	0.431	
P-VAL	0.67		0.015		
CHAIN: LYTEIMBAL → ACIDOSIS → O2DIFFDYS → COAG					
	2018		2019		
	SEP	NON-SEP	SEP	NON-SEP	
COUNT	4	4	6	7	
	5	18	5	23	
RATIO	0.444	0.181	0.545	0.233	
P-VAL	0.184		0.072		